Ultra-small-angle X-ray scattering at the Advanced Photon Source
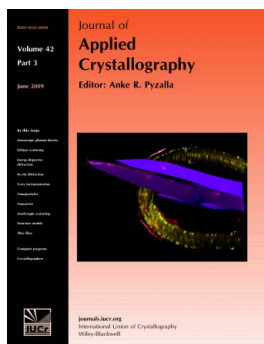
Jan Ilavsky, Pete R. Jemian, Andrew J. Allen, Fan Zhang, Lyle E. Levine and Gabrielle G. Long

Many research topics in condensed matter research, materials science and the life sciences make use of crystallographic methods to study crystalline and non-crystalline matter with neutrons, X-rays and electrons. Articles published in the *Journal of Applied Crystallography* focus on these methods and their use in identifying structural and diffusion-controlled phase transformations, structure–property relationships, structural changes of defects, interfaces and surfaces, *etc.* Developments of instrumentation and crystallographic apparatus, theory and interpretation, numerical analysis and other related subjects are also covered. The journal is the primary place where crystallographic computer program information is published.

Crystallography Journals Online is available from **journals.iucr.org**

Ultra-small-angle X-ray scattering at the Advanced Photon Source

Jan Ilavsky,[a]* Pete R. Jemian,[a] Andrew J. Allen,[b] Fan Zhang,[a] Lyle E. Levine[b] and Gabrielle G. Long[a]

[a]Advanced Photon Source, Argonne National Laboratory, Argonne, IL 60439, USA, and [b]Materials Science and Engineering Laboratory, National Institute of Standards and Technology, Gaithersburg, MD 20899, USA. Correspondence e-mail: ilavsky@aps.anl.gov

The design and operation of a versatile ultra-small-angle X-ray scattering (USAXS) instrument at the Advanced Photon Source (APS) at Argonne National Laboratory are presented. The instrument is optimized for the high brilliance and low emittance of an APS undulator source. It has angular and energy resolutions of the order of 10^{-4}, accurate and repeatable X-ray energy tunability over its operational energy range from 8 to 18 keV, and a dynamic intensity range of 10^8 to 10^9, depending on the configuration. It further offers quantitative primary calibration of X-ray scattering cross sections, a scattering vector range from 0.0001 to 1 Å^{-1}, and stability and reliability over extended running periods. Its operational configurations include one-dimensional collimated (slit-smeared) USAXS, two-dimensional collimated USAXS and USAXS imaging. A robust data reduction and data analysis package, which was developed in parallel with the instrument, is available and supported at the APS.

1. Introduction

Small-angle X-ray scattering (SAXS) is a nondestructive measurement technique in which the elastic scattering of X-rays from inhomogeneities within a sample is recorded at low scattering angles. SAXS data contain information about parameters such as the size, shape, volume and total surface area of the scatterers, as well as the characteristic distances between those scatterers that are ordered or partially ordered. The typical range of scattering angles in a pinhole SAXS camera delivers structural information on length scales between 1 and 100 nm. To resolve microstructures with larger dimensions, however, the smaller angles available with ultra-small-angle X-ray scattering (USAXS) are required. An added benefit of USAXS is that a broader size range can be accessed, albeit with lower efficiency for the smaller sizes.

USAXS instruments are traditionally based on the original Bonse–Hart double-crystal configuration (Bonse & Hart, 1965), which utilized multiple dispersive reflections from perfect crystals to reach a region of scattering vector **q** [where its modulus $q = (4\pi/\lambda)\sin\theta$, λ is the wavelength of the X-ray and 2θ is the scattering angle] that is generally 'behind the beam stop' in the pinhole SAXS configuration. They achieve high-angular resolution as a result of the narrow angular width of the crystal (Darwin) rocking curve. Multiple reflections from the collimating crystal pair and the analyzing crystal pair (see Figs. 1 and 2) reduce the wings of the instrumental rocking curve to improve the signal-to-noise ratio. By making use of an optimal detector, a nondispersive geometry and appropriate scanning motions, the Advanced Photon Source

(APS) USAXS instrument extends the capabilities of USAXS by delivering sensitivity over more than three decades (from below 1 nm to above 1 μm) in size in a single scan.

USAXS instruments have made use of a variety of X-ray sources: a laboratory source (Rieker & Hubbard, 1998), second-generation synchrotron X-ray sources (Long et al., 1991; Chu et al., 1992, 1994; Smolsky et al., 2007; Krosigk et al., 2001) and third-generation synchrotron X-ray sources (Narayanan et al., 2001; Ilavsky et al., 2003). In addition, making use of a very long (> 200 m) sample-to-detector distance, pinhole SAXS can reach scattering angles comparable to the low-q limit of a Bonse–Hart camera (Shinohara et al., 2007). It has been lately reported that analysis of near-field speckle (Cerbino et al., 2008) provides access to the low-q region, though with limitations.

We mention also several ultra-small-angle neutron scattering (USANS) instruments (Schwahn & Koo, 1986; Schwahn et al., 1985; Barker et al., 2005; Hainbuchner et al., 2000; Borbely et al., 2000; Aizawa & Tomimitsu, 1995; Aizawa & Arai, 2006; Agamalian et al., 1998) that are based on the Bonse–Hart concept. A USANS instrument at the Spallation Neutron Source at Oak Ridge National Laboratory is projected to allow measurements in a range of length scales from 100 nm to 200 μm (Carpenter et al., 2003). This capability, together with the high peak flux that the pulsed neutron source will offer, is expected to represent the future state of the art in USANS.

In this paper, we describe the USAXS instrument at the APS at Argonne National Laboratory, constructed in partnership with the National Institute of Standards and Tech-

nology, Gaithersburg, MD, USA. This instrument allows measurements not previously possible, especially in the case of low photon counting statistics for samples with low scattering contrast. The instrument utilizes optics that have been optimized for the low-emittance source, a detector and associated electronics that are linear over ten decades of photon intensity, and ancillary scanning motions that deliver access to an extended q range. As detailed in the sections that follow, it achieves high angular and energy resolution, accurate energy tuning, excellent signal-to-noise ratio, and the quantitative primary calibration of the X-ray scattering cross section. Measurements can be performed with standard one-dimensional collimated USAXS, two-dimensional collimated USAXS, quantitative anomalous USAXS even in the presence of copious fluorescence, selected-area USAXS and USAXS imaging. This portfolio of capabilities enables the characterization of microstructures nominally between 1 nm and 1 µm *via* scattering, and above 1 µm *via* imaging. With these attributes, it serves to bridge the important region between pinhole SAXS or SANS and small-angle light scattering (Allen *et al.*, 1994; Schaefer *et al.*, 2003).

We introduce the operation of the APS USAXS in §2. In §§3 and 4, beamline control, especially the data acquisition process, and the operational configurations are described. We briefly discuss the data reduction and data analysis processes in §§5 and 6. Science examples are highlighted in §7 to demonstrate the performance and capabilities of the APS USAXS instrument, and concluding remarks are offered in §8.

2. Beamline configuration

A schematic of the APS USAXS instrument is shown in Fig. 1. The instrument is located at X-ray Operations and Research (XOR) Sector 32, where it receives photons from an APS Undulator A (Lai *et al.*, 1993). An APS Undulator A provides continuous access to X-rays in the range from 3.2 to 80 keV and above. The photons subsequently pass through a fixed-offset Si (111) monochromator, capable of tuning the photon energy between 8 and 35 keV. With incident white-beam radiation, the monochromator selects not only the primary photon energy of interest but also photons with higher-order harmonic energies. To reject the unwanted higher-order harmonics, a pair of vertically reflecting, flat, 350 mm-long silicon mirrors in a nondispersive (1, −1) orientation follow the monochromator. The mirrors have three stripes, Si, Cr and Rh, each with a different angular dependence on X-ray energy for total reflection. By means of a simple horizontal translation to select the appropriate reflection stripe, the mirrors reject harmonics for primary photons in the energy range from 8 to 19 keV, which is the operational range of the APS USAXS. At 8 keV, the rejection of higher harmonic radiation is better than 1 part in 10^6.
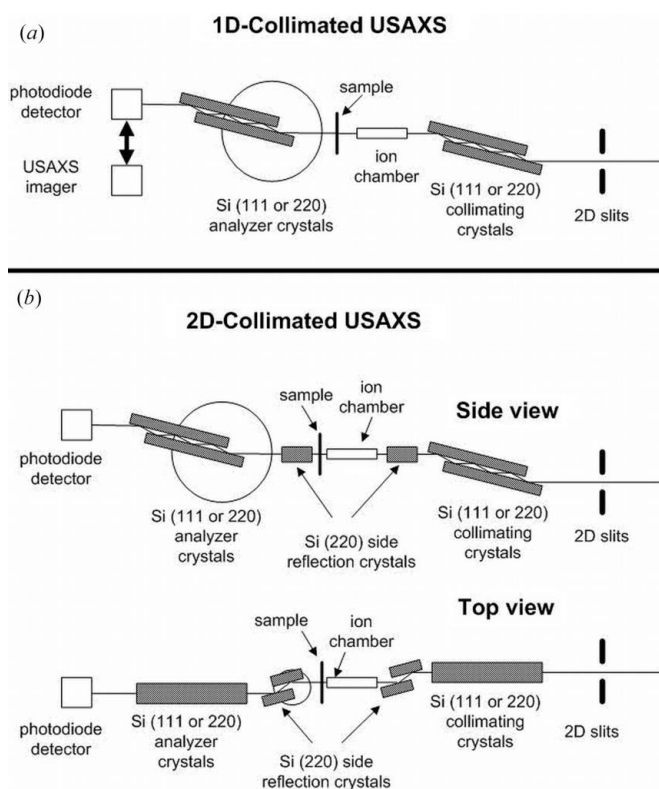

Figure 1
Schematic of the APS USAXS instrument in (*a*) one-dimensional collimated or USAXS imaging configuration, and (*b*) two-dimensional collimated configuration (viewed from the top and from the side). Synchrotron radiation enters from the right, passing through a high-heat-load monochromator and then harmonic rejection mirrors before reaching the USAXS two-dimensional entrance slits.
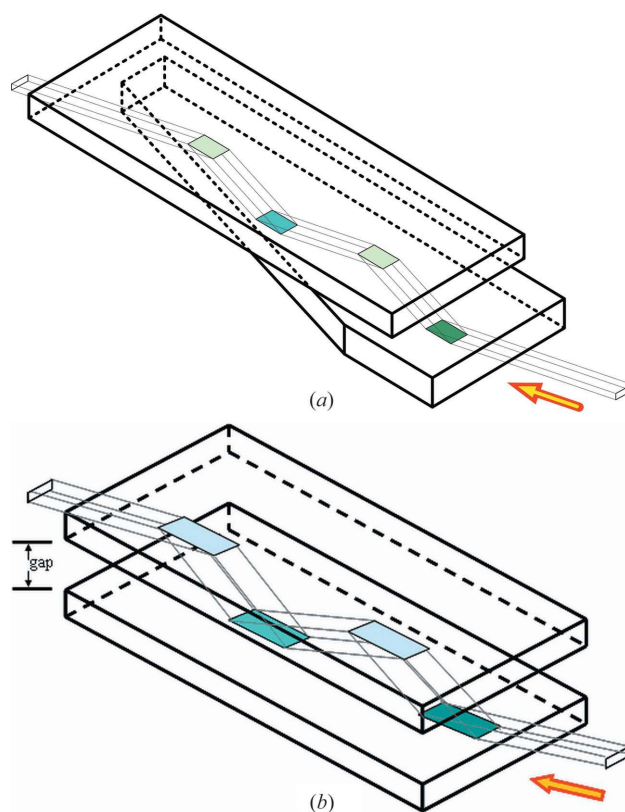

Figure 2
(*a*) Fixed-gap USAXS collimating crystals and (*b*) variable-gap USAXS analyzer crystals.

Control of the incident X-ray beam intensity and of the beam size is available *via* pneumatically controlled Al, Ti or glass attenuators (filters) and two-dimensional beam-defining, high-resolution (approximately 10 nm precision) slits. Parasitic scattering from these filters and slits is removed by USAXS collimating crystals. The USAXS instrument vertical collimation is implemented with a pair of fixed-gap, 150 mm-long × 25 mm-wide Si (111) or (220) crystals. Unlike the original and widely adopted design of Bonse and Hart (Bonse & Hart, 1965, 1966; Narayanan *et al.*, 2001; Barker *et al.*, 2005), which used an odd number of reflections from the collimating crystals, we use an even number of reflections [2, 4, 6 or 8 reflections for Si (111), or 2, 4 or 6 reflections for Si (220)] in a nondispersive geometry. The rocking curve wings fall off as q^{-2n} in the scanning direction, where n is the number of reflections in the crystal pair. In this manner, a large number of reflections deliver an optimized signal-to-noise ratio. Furthermore, a narrow crystal gap, combined with the many reflections, prohibits the direct (uncollimated) beam from reaching the sample. Finally, the vertically collimated nondispersive geometry, with an even number of reflections, offers the benefits of a more compact instrument, simpler mechanical motions, better stability and reproducibility, and easier access to a broad range of X-ray energies than is possible with dispersive designs.

The collimating crystals make use of a design (Ilavsky *et al.*, 2003) illustrated in Fig. 2(*a*), where the triangular cut of the first crystal makes it possible to select the number of reflections by translating the crystal pair horizontally. Each collimating crystal is independently precision mounted on a three-point kinematic magnetic mount attached to a sub-micro-radian-resolution rotational stage. As for the analyzer crystals shown in Fig. 2(*b*) and discussed below, the alignment of the collimating crystal pair is further controlled by means of an overconstrained weak-link mechanism (Shu *et al.*, 2001). A picomotor and a piezoelectric transducer serve as actuators, and a separate picomotor serves for tilt adjustment. Finally, the collimating crystals are enclosed in a nitrogen-gas environment to reduce the likelihood of oxidation of the crystal surfaces. The quality of the crystal surfaces is key to ensuring that the wings of the instrumental rocking curve are effectively suppressed over the large q range for data acquisition. Although the alignment of the collimator crystals typically does not drift over a span of many hours, automatic optimization of the motor positions is implemented to ensure robust operation of the collimator. The measured throughput of the collimating crystal pair with six reflections and 10 keV incident radiation on Si (111) is better than 50%, and with a typical X-ray beam size of 0.4 mm vertical × 2.0 mm horizontal, the USAXS instrument receives ~10^{13} photon s^{-1} at the sample position.

2.1. One-dimensional collimated USAXS optics

In the one-dimensional collimated USAXS configuration, shown schematically in Fig. 1(*a*), a windowless ionization chamber after the collimating crystals monitors the X-ray intensity reaching the sample position. With no X-ray window, this detector delivers an accurate measure of the X-ray beam without introducing parasitic scattering.

The scattering sample is mounted on a stand-alone stage with two motorized orthogonal translational axes. This allows samples to be attached to a sample-mounting plate and measured in sequential order. The resolution of the linear stages (0.5 μm) enables different regions of an inhomogeneous sample to be probed locally. Ample space around the sample stage makes possible the installation of sample environments such as heating stages, flow cells (Allen *et al.*, 2008), flame chambers (Kammler *et al.*, 2004), tensile stages (Long & Levine, 2005) and liquid cells.

The vertically diffracting analyzer crystals are a pair of Si (111) crystals or Si (220) crystals with the same crystallographic orientation and number of reflections as the collimating crystals. They are each mounted on a high-precision rotational stage, similar to the mounts for the collimating crystals, except that the number of reflections is selected by varying the crystal gap (Fig. 2*b*). By not using channel-cut crystals for the collimating and analyzing pairs, it is easy to avoid accidental diffractions by rotating slightly the second crystal in the pair about the diffraction vector. The stability of the analyzer pair is maintained with a second high-stiffness weak-link rotary stage. The X-ray throughput of the analyzer crystals can be as high as 90%.

The analyzer rotational stage is equipped with a high-resolution, high-accuracy optical angular encoder that defines the measured scattering vector. The analyzer crystal rotation angle ϑ is related to the scattering angle 2θ as $\vartheta - \vartheta_c = 2\theta$, where ϑ_c is the center of the analyzer crystal rocking curve. We typically rotate the analyzer crystals in logarithmic q steps, as this corresponds to the physics of scattering and also covers a wide q range efficiently. Logarithmic stepping is shown in Fig. 3; it is implemented by taking the smallest angular step size $\Delta\vartheta_{min}$ when traversing the rocking curve peak, and taking approximately proportionately larger steps as the angular distance from the peak position ϑ_c increases. The step size is given by

$$\Delta\vartheta_{i+1} = \Delta\vartheta_{min} + k|\vartheta_i - \vartheta_c|^\eta. \qquad (1)$$

For $\eta = 1$, equal log-spaced q steps are taken in the wings of the rocking curve, while constant-sized steps are taken in the vicinity of ϑ_c. As η increases, larger steps are taken in the wings of the rocking curve (thereby compressing points near ϑ_c). Typically, $\eta \simeq 1.2$ gives good results. For a target scan of N points distributed between ϑ_{start} and ϑ_{end}, we define the first value $\vartheta_1 = \vartheta_{start}$. The parameter k is adjusted by minimizing the error in arriving at the final step ϑ_N, so that $|\vartheta_N - \vartheta_{end}| \leq \Delta\vartheta_{min}/2$. When fine features, such as small oscillations or sharp low-angle diffraction peaks, are present in the scattering curve, we use linear q steps at or close to $\Delta\vartheta_{min}$ to guarantee that structural information is adequately mapped.

In addition to the rotation of the analyzer crystals during a USAXS scan, the entire analyzer stage is scanned downwards
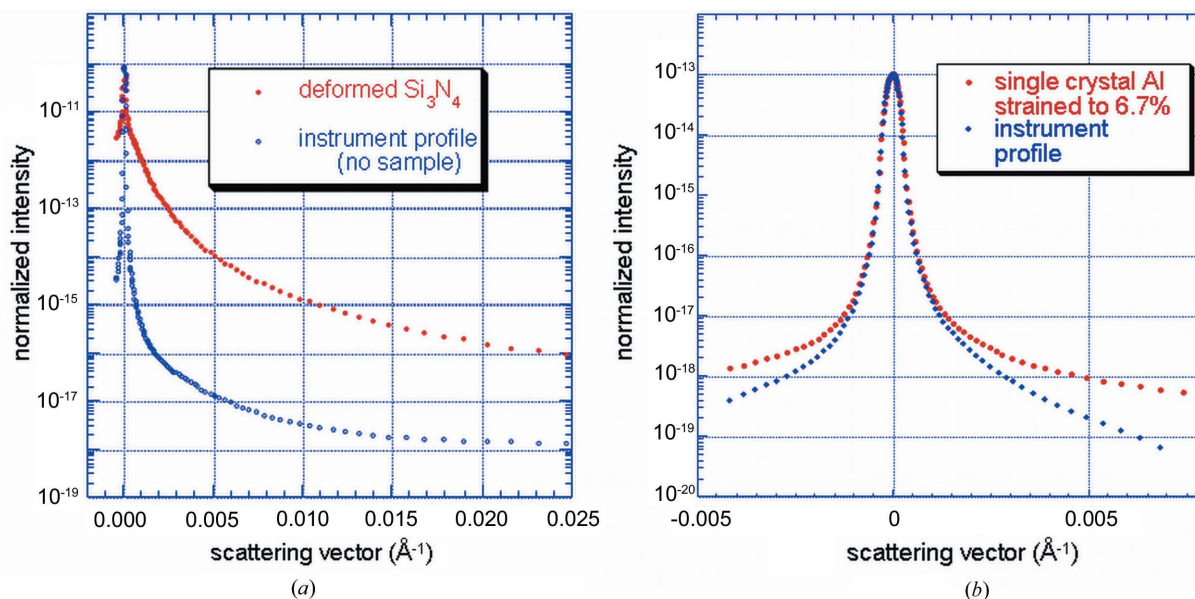
Figure 3
Examples of raw data from the USAXS demonstrating the q-step algorithm. (a) Data for a weakly scattering sample (red) showing the lowest q where the sample scattering becomes significantly larger than the instrumental curve (blue). (b) Data for a strongly scattering sample (red) and instrument curve (blue) showing the increasing q step size as q increases. In both (a) and (b) the sample scattering was adjusted for transmission.

by an amount equal to $SA \times \tan(\vartheta - \vartheta_c)$, where SA is the sample-to-analyzer distance. This ensures that the Bragg reflection of X-rays scattered at the q value defined by the analyzer rotation remains centered on the crystals.

Appendix A in the supplementary material[1] provides more detailed information on the crystal Darwin rocking curve profile in q as it relates to USAXS measurements.

The USAXS crystal surfaces undergo a strict polishing and etching procedure. After mechanical polishing, small strained regions may remain close to the crystal surface even though the surface may appear perfectly flat. These strains introduce parasitic scattering into the scattering profile, especially at the high-q end where the signal-to-noise ratio is low (Agamalian *et al.*, 1998; Sztucki *et al.*, 2008). With one deep etching treatment after the polishing and a few cycles of alternate chemomechanical polish and light etching treatments, the parasitic scattering is much reduced and the crystal surfaces satisfy the requirements of USAXS measurements. We note that this procedure still does not satisfy the requirements for USAXS imaging, where the etched surface distorts the X-ray wavefront and consequently the imaging measurements. Additional light etch and light polish treatments are needed to make the crystal surfaces as strain-free as possible for USAXS imaging.

2.2. Two-dimensional collimated USAXS optics

For two-dimensional collimated USAXS, shown schematically in Fig. 1(b), a 25 mm-high, horizontally reflecting channel-cut crystal is mounted on a rotational stage and installed after the vertically reflecting collimating crystal pair

and before the ionization chamber. In this manner, the X-ray beam incident on the sample is collimated both vertically and horizontally. Another horizontally reflecting channel-cut crystal pair is installed after the sample and before the vertically reflecting analyzer crystals. Each of these channel-cut crystal pairs is Si (220) and makes use of only two reflections. The horizontally reflecting analyzer crystal pair selects the $q_x = 0$ beam after the sample. The placement of the horizontally reflecting analyzer crystal pair before the vertically reflecting analyzer crystal pair avoids adjustments for the vertical displacement caused by scanning of q. Nevertheless, the horizontally reflecting analyzer crystal pair must still be rotated slightly about its vertical axis during a two-dimensional collimated USAXS scan by an amount equal to $\{\tan^{-1}[\tan\vartheta_B \sec(\vartheta - \vartheta_c)] - \vartheta_B\}$ to ensure that the Bragg condition ϑ_B is satisfied for X-rays at increasing q as their downward scattering trajectory increasingly diverges from the horizontal beam direction.

2.3. USAXS imaging

The USAXS imaging geometry is based upon the one-dimensional collimated USAXS configuration (Fig. 1a). However, USAXS imaging makes demands on the instrument that are different from those of one-dimensional or two-dimensional collimated scattering. First, the imaging crystals must be flat and strain-free so as to eliminate wave distortion caused by surface roughness. The number of reflections in the collimator and analyzer is limited to two. Finally, USAXS imaging is typically operated in a very compact geometry, in which the sample, detector and analyzer are brought as close together as possible to maximize spatial resolution. The details

of the geometry can be found elsewhere (Levine & Long, 2004).

2.4. Detector stage

The USAXS detector and USAXS imaging camera are both mounted on a detector stage equipped with precision translational motions in two orthogonal directions. The minimum translation step size is 2.5 µm. The USAXS photodiode detector (Jemian & Long, 1990) and the associated electronics deliver linear response, high quantum efficiency, high signal-to-noise ratio, low cost and long lifetime in the X-ray beam. Most notably, this linearity over the entire range of photon counting rates enables the reliability, reproducibility and extended q range of the USAXS instrument. The USAXS imaging camera is a CCD behind an X-ray-to-visible fluorescent YAG crystal and an objective lens (Levine & Long, 2004; Long *et al.*, 2001). The effective pixel size of the image detection system is 0.45 µm with a $20\times$ objective lens. The image resolution is limited by the X-ray-to-optical conversion and fundamental limits in the optical imaging system; in practice, it reaches just below 1 µm. For higher spatial resolution, fine-grain (0.17 µm) nuclear emulsion plates can be used (Long *et al.*, 2001; Levine & Long, 2004). A 6 µm resolution, real-time X-ray video camera is the third device mounted on the detector stage. This camera is used for orienting samples by means of radiography (at $q = 0$) and low-resolution USAXS imaging ($q > 0$), and for fast and reliable alignment of the instrument.

3. Instrument control

Instrument control and data acquisition are conducted through *spec* macro commands (Swislow, 2009), layered on top of EPICS (Dalesio *et al.*, 1993). Its operation includes a user-

friendly graphical user interface where every motor is controlled *via* computer in the workstation. Macros have been written to perform routine tasks, such as tuning the collimating crystals and the analyzer crystals. One can, for example, switch from radiography (with real-time camera) to USAXS operation (with photodiode detector) by means of a single command. Samples are typically examined radiographically and *via* USAXS imaging beforehand so that macroscopically inhomogeneous or damaged regions, if present, can be avoided. Sample positions are recorded in a batch file, where the USAXS scans from these samples are then automatically completed accordingly. A USAXS scan with 150 data points over the peak of the rocking curve and subsequently covering a q range from 1×10^{-4} to $1\ \mathring{A}^{-1}$, with 5 s data collection time for each point, is completed within 15 min. If a smaller q region is of interest, a fast USAXS scan can be acquired in a few minutes. In this manner, the instrument offers limited time-resolved measurements for the investigation of slow kinetics.

The data are recorded in a *spec* file where they are ready to be reduced to a standard data format of absolute calibrated and desmeared scattering cross section *versus* q. Thus, USAXS reduced data can be readily combined with complementary light scattering and/or pinhole SAS data.

4. Operational configurations

In this section, we first discuss the three USAXS configurations, and then we briefly describe anomalous USAXS and selected-area USAXS.

4.1. One-dimensional collimated USAXS

The one-dimensional collimated USAXS configuration is the optimal geometry for measuring low-angle scattering over a large q range (1×10^{-4} to $1\ \mathring{A}^{-1}$) from an isotropic sample area up to 1 mm high $\times$ 2 mm wide. A single scan can deliver nine decades in intensity of absolutely calibrated scattering data. The total usable q range also varies with the strength of scattering from a sample for both high-q and low-q regions (Fig. 3).

In the one-dimensional collimated USAXS configuration, the analyzer crystals select the scattered X-rays based only on the modulus of the vertical momentum transfer or q component. The scattering geometry is shown in Fig. 4. The angle in the scanning direction is highly collimated by the optics because the slit width in units of q, $2w_0$, along the scanning direction is the FWHM of the rocking curve with no sample in the beam. The angular slit length in units of q in the horizontal direction is $2l_0$ and is not restricted by the optics. The angular slit length is determined instead by the geometry, *i.e.* the angular size of the photodiode detector subtended at the sample position. With a detector diameter of 5.5 mm and a sample-to-detector distance SD of several hundreds of millimetres, $2l_0$ is very much greater than $2w_0$.

Appendix B in the supplementary material describes requirements for the minimum sample-to-detector distance,
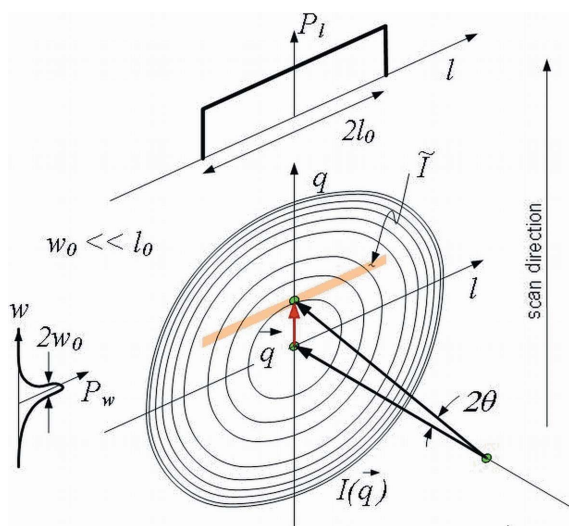

Figure 4
Schematic of finite slit scanning. 2θ is the scattering angle, $2l_0$ is the slit length, $2w_0$ is the slit width and $q = (4\pi/\lambda)\sin\theta$ is the scattering vector. P_1 is the slit-length weighting function, and P_w is the slit-width weighting function.

Jan Ilavsky *et al.* · Ultra-small-angle X-ray scattering

Table 1
Comparison of one-dimensional and two-dimensional collimation geometries.

	One-dimensional collimated USAXS	Two-dimensional collimated USAXS
Side-reflection crystals	No	Yes
Desmearing	Yes	No
Type of scatterers	Isotropic	Anisotropic
q range Si (111)	1.4×10^{-4} to 1 Å^{-1}	1.4×10^{-4} to 0.1 Å^{-1}
q range Si (220)	1.0×10^{-4} to 1 Å^{-1}	1.0×10^{-4} to 0.1 Å^{-1}
Intensity range	Up to nine decades of intensity (after desmearing)	Up to eight decades
Maximum beam size	1.0×2.0 mm	0.4×0.4 mm

coupled with the maximum allowable tolerances on the mutual tilt angle of the two analyzer crystals.

If the scattering sample is isotropic, the scattering intensity $I(\mathbf{q}) = I(q)$ and the smearing caused by the finite slit length and width can be calculated and recovered from the data (Long *et al.*, 1991). Given that the angular slit width is so small, correction for it is negligible, and so this step is omitted. The angular slit length, however, can be large compared with the scattering angle 2θ. Correction ('desmearing') of these slit-smeared data is therefore required and is carried out iteratively (Lake, 1967; Jemian, 1990).

4.2. Two-dimensional collimated USAXS

Even though there are many advantages of one-dimensional collimated USAXS measurements, one cannot recover the true scattering from slit-smeared USAXS data when the sample (and therefore the scattering) is anisotropic. To overcome this limitation, two-dimensional collimated USAXS is required.

In the two-dimensional collimated USAXS configuration, the maximum X-ray beam size is reduced to 0.4×0.4 mm, and the sample is mounted on a stage capable of rotating the sample azimuthally about an axis parallel to the instrument beam direction. Two orthogonal translational stages center the azimuthal rotation in the X-ray beam, and an additional linear stage centers the sample on the azimuthal rotation. Both sets of analyzer crystals and the azimuthal rotation can be scanned. The anisotropic scattering profile can be recorded in two ways. (1) The azimuthal angle α is fixed and the scattering intensity is measured as q is scanned. A two-dimensional map is obtained by stepping α and repeating the q scan. (2) The scattering vector q is fixed and the scattering intensity is measured as the azimuthal angle α is scanned. A two-dimensional map is constructed by stepping q and repeating the α scan.

Although two-dimensional collimated USAXS is available in the same X-ray energy range as one-dimensional collimated USAXS, the two-dimensional scattering vector range is limited to the range between $q = 1 \times 10^{-4}$ Å^{-1} and $q = 0.1$ Å^{-1}, owing to reduced X-ray intensity from the addition of horizontal-reflection collimating and analyzer crystals. The instrument can record anisotropic scattering patterns just as a

pinhole camera can, but two-dimensional collimated USAXS reaches into an inaccessible low-q realm with higher q resolution and arbitrarily fine azimuthal angular resolution that is not possible with pinhole cameras. A comparison of one-dimensional and two-dimensional collimated USAXS is shown in Table 1.

4.3. USAXS imaging

USAXS imaging is an imaging modality that utilizes small-angle X-ray scattering as the contrast mechanism (Levine & Long, 2004). The SAXS contrast mechanism provides inherently high-contrast images of density variations within a sample. This makes USAXS imaging particularly useful when absorption and phase contrast are very low. USAXS imaging extends the range of USAXS characterization from length scales just below 1 µm up to the full size of the X-ray beam, and quantifies spatial inhomogeneities inside the sample volume. It has been used to investigate systems ranging from polymeric composite materials (Levine *et al.*, 2007) to plastically deformed metals (Long *et al.*, 2001).

Although the imaging geometry is not optimal for USAXS measurements, one-dimensional collimated USAXS scans can be conducted. Thus, high-resolution USAXS images at low-q scattering vectors, which can be acquired almost in real time, allow informed decisions to be made regarding the scattering features of interest. Area-selection slits can be moved in and a USAXS scan can be acquired from the selected area, thereby coupling directly the image with information on the underlying microstructure. Finally, low-resolution USAXS images can easily be acquired in the conventional one-dimensional collimation USAXS geometry where they are used for sample characterization prior to conducting USAXS scans.

The image contrast of USAXS imaging has been explained quantitatively by making use of phase propagation and dynamic diffraction theory (Zhang, Long, Levine *et al.*, 2008). Simulated results from a model system of micrometre-sized, spherical SiO$_2$ particles embedded in a polypropylene matrix show good agreement with experimental measurements. Simulations by means of an alternative geometric ray-tracing method also account for the features in the USAXS images, and offer a complementary view of the small-angle X-ray scattering contrast mechanism. The ray-tracing analysis indicates that refraction, in the form of Porod scattering, and, to a much lesser extent, X-ray reflection, fully account for USAXS image contrast.

4.4. Anomalous USAXS and selected-area USAXS

USAXS is an optimal technique for anomalous scattering measurements near absorption edges (Jemian, 1990) with an energy resolution $\Delta E/E \simeq 0.00015$, a primary calibration of the scattered intensity on an absolute scale, and an ability to measure scattering without interference from copious fluorescence. An automated anomalous USAXS (A-USAXS) control macro adjusts the photon energy by tuning the upstream undulator and monochromator, realigning the entire instrument, and collecting data in sequential order. A set of

one-dimensional collimated A-USAXS measurements at six X-ray energies near an absorption edge can be completed in less than 3 h. The high stability of the USAXS instrument and the ease with which we can adjust the energy reliably and reproducibly make A-USAXS a routine function.

Since the sample position is highly stable, the high-resolution beam-defining slits can be used to reduce the beam size down to 20 µm in one direction to facilitate selected-area USAXS. In this manner the USAXS instrument operates as a microprobe, measuring sample variations and microstructures in the vicinity of interfaces. However, the beam intensity at small dimensions is greatly reduced ($I_{\Delta x, \Delta y} = 1.0 \times 10^{13} \Delta x \Delta y$ photon s^{-1}, where Δx and Δy are the slit openings in mm along the horizontal and vertical directions, respectively). Furthermore, as the slit opening approaches $2\pi/q$, data interpretation becomes complicated. Based on these considerations, the slit opening should not be smaller than 15×200 µm for selected-area USAXS.

5. Data reduction

An *IgorPro*-based[2] data reduction package (*Indra*) has been developed, verified and established for fast and accurate data reduction of USAXS data (Ilavsky & Jemian, 2009). The data reduction process consists of several standard steps such as absolute calibration, desmearing (one-dimensional collimated USAXS) and corrections for multiple scattering.

The scattering intensity $I(q)$ (Long *et al.*, 1991) is

$$I(q) = I_0 t T \varepsilon \Omega \frac{\mathrm{d}\Sigma}{\mathrm{d}\Omega}(q), \qquad (2)$$

where I_0 is the incident X-ray intensity, t is the sample thickness, T is the sample transmission, ε is the efficiency of the detector, Ω is the detector solid angle and $\mathrm{d}\Sigma(q)/\mathrm{d}\Omega$ is the differential scattering cross section per unit volume per unit solid angle. We define the sample transmission T (< 1) as the attenuated fraction of the incident beam intensity that passes through the sample, where the attenuation includes all processes except for small-angle scattering. Note that, while this is a commonly used definition, it is not universal (see, for example, Schelten & Schmatz, 1980; Cotton, 1991). The detector efficiency ε is constant over the entire intensity range, and the solid angle Ω subtended by the detector is given by $\Omega = 2\vartheta_w 2\vartheta_l$ (Fig. 4); $2\vartheta_w$ is the width of the rocking curve of the silicon optics measured at half the peak intensity (also known as the FWHM) and $2\vartheta_l = D_{PD}/(2SD)$, where D_{PD} is the diameter of the photodiode detector and SD is the distance between the sample and the detector. Absolute calibration of the scattering cross section depends only on the known quantities t, T, Ω and I_0: t can be measured, T can be deduced from the ratio of the peak intensity with and without the

sample in the beam, I_0 can be measured with no sample in the beam with the analyzer set to $q = 0$, and Ω can be calculated from the definition above.

The next step in data reduction for one-dimensional collimated USAXS is the correction for slit smearing. As indicated earlier, correction for slit width is negligible, and so a modified algorithm that corrects only for the slit length was developed (Jemian, 1990); this can be found in the data reduction package (Ilavsky & Jemian, 2009). Slit smearing of one-dimensional USAXS data is described by

$$\frac{\mathrm{d}\tilde{\Sigma}}{\mathrm{d}\Omega}(q) = \frac{1}{l_0} \int_0^{l_0} \frac{\mathrm{d}\Sigma}{\mathrm{d}\Omega}(q^2 + l^2)^{1/2} \, \mathrm{d}l, \qquad (3)$$

where $\mathrm{d}\tilde{\Sigma}(q)/\mathrm{d}\Omega$ is the measured, slit-smeared scattering intensity; $\mathrm{d}\Sigma(q)/\mathrm{d}\Omega$ is the unsmeared scattering cross section; and l is the reciprocal vector of integration in the slit direction.

In practice, each USAXS sample scan of $I(q)$ is derived from scans of the scattering profile with the sample in the beam $R(q)$ and the corresponding blank with no sample in the beam $R_0(q)$ over the same q range (Fig. 3). The sample transmission (measured at $q = 0$) is available from the ratio $T = R(0)/R_0(0)$ and is used to normalize the sample scattering for subtraction of the instrument contribution. Thus the measured, slit-smeared scattering intensity above is

$$\frac{\mathrm{d}\tilde{\Sigma}}{\mathrm{d}\Omega}(q) = \left[\frac{R(q)/T - R_0(q)}{R_0(q = 0)} \right] \frac{1}{t\Omega}. \qquad (4)$$

The presence of multiple scattering in either one-dimensional or two-dimensional collimated USAXS is typically detected by the observation of apparent broadening of the rocking curve when the sample is in the X-ray beam. In this case, the transmission ratio defined above is not a correct measure of the sample transmission because a significant part of the attenuation is due to small-angle scattering itself. Therefore, a multiple scattering correction is required to obtain the true absolute intensity calibration. To achieve this, the transmission is calculated instead from the ratio of the integrated intensity for the sample scan divided by the integrated intensity for the blank scan near $q = 0$ where multiple scattering is apparent. This procedure does not correct for distortions in the shape of $I(q)$ in the multiple-scattering-affected q range, but it does correct for the transmission and hence gives an accurate absolute calibration for the data at larger q values.

6. Data analysis

A tool suite called *Irena* (Ilavsky & Jemian, 2009) was developed for the analysis of X-ray and neutron small-angle scattering (SAS) data, within the commercial *IgorPro* application; this suite is now supported at the APS and is available to SAS researchers. *Irena* brings together a comprehensive set of tools for materials science, materials physics, chemistry, polymer science and other fields. In addition to the derivation of the standard Guinier and Porod fits, the suite includes size distribution determination in the dilute limit using maximum

---

[2] Certain commercial equipment, instruments, software or materials are identified in this paper to foster understanding. Such identification does not imply recommendation or endorsement by the Department of Commerce or the National Institute of Standards and Technology, nor does it imply that the materials or equipment identified are necessarily the best available for the purpose.
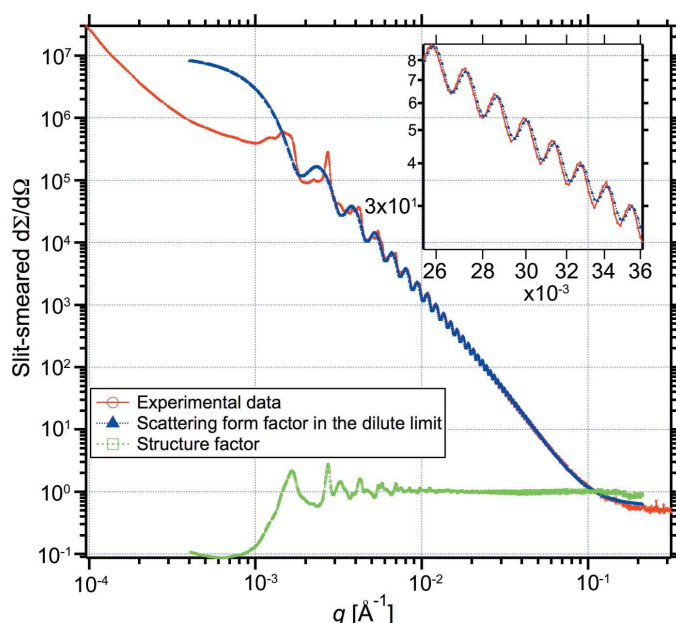
Figure 5
Scattering from monodisperse silica beads, shown in red. A least-squares fit to the high-q region of the scattering curve, in blue, is dominated by the single-particle form factor. The structure factor, in green, is calculated by dividing the red scattering curve by the blue form factor curve.
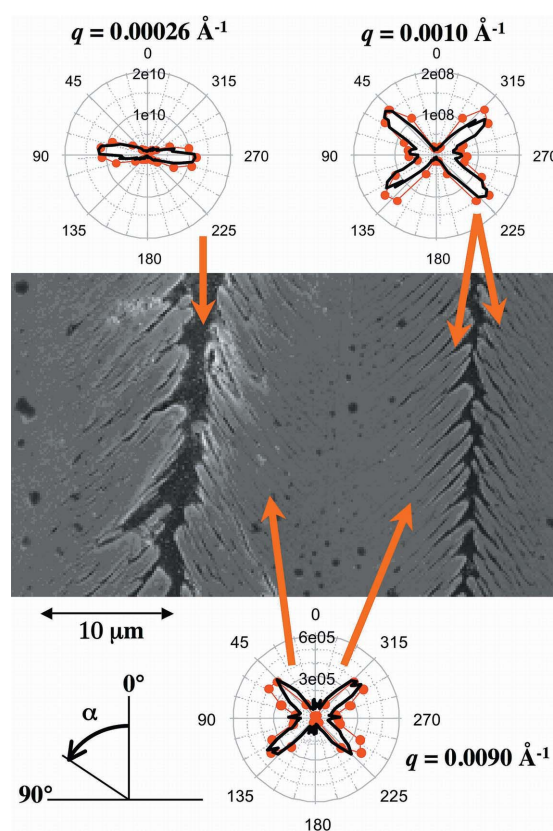

Figure 6
Scanning electron microscopy image of a sectioned EB-PVD YSZ coating showing the associated measured and predicted scattering intensities (respectively, the black lines and the red lines with spots in each polar plot) as a function of the azimuthal angle, α (in degrees), for $q = 0.00026$, 0.0010 and 0.0090 Å^{-1}. The direction at $\alpha = 0°$ is perpendicular to the substrate plane. Note the strong differences in anisotropy at different q within this single sample. The thick arrows indicate how the anisotropies are related to the microstructural features at different length scales. The standard deviation uncertainties in the anisotropic data are smaller than the thickness of the lines plotted.

entropy (Potton *et al.*, 1988) and other methods; modeling of dilute-limit small-angle scattering from multiple non-interacting populations of scatterers; unified fits (Beaucage, 1995); Debye–Bueche modeling (Debye & Bueche, 1949); pair distance distribution functions; reflectivity analysis using Parrat's formalism (Parratt, 1954); and a low-angle diffraction tool. The suite is implemented together with support tools such as data import/export for a range of common data formats, data modification, presentation-quality graphics optimized for small-angle scattering data, and an X-ray and neutron contrast calculator. *Irena* contributes significantly to the scientific productivity of the APS USAXS facility. At this time, *Irena* is available for both Windows and Mac operating systems.

7. Instrument performance and scientific application

In this section, we offer several examples to illustrate the performance and capabilities of the APS USAXS.

7.1. Crystal rocking curve measurement

The rocking curve measurement determines the $q = 0$ position and determines the quality of the absolute calibration. As noted above, Appendix A in the supplementary material provides more detailed information on the crystal Darwin rocking curve profile in q as it relates to USAXS measurements.

7.2. Scattering from monodisperse silica beads

The USAXS instrument high-q resolution enables fine features to be resolved easily. Fig. 5 shows the scattering

profile of monodisperse silica beads. The oscillations resulting from the form factor of a perfect sphere go all the way out to the high-q end of the USAXS range. The inset shows a magnified curve near $q = 3 \times 10^{-2}$ Å^{-1} where the oscillations are still clearly visible. The blue curve in Fig. 5 shows a least-squares fit of the high-q region of the curve, where the scattering is dominated by the single-particle form factor. If we divide the red scattering curve by the blue form factor curve, a structure factor, which is the Fourier transform of the density–density correlation function, is obtained. The density–density correlation function contains information about two-body interparticle correlation and is available for analysis or comparison to known or perceived interparticle potentials.

7.3. Anisotropic USAXS

We show in Fig. 6 the two-dimensional collimated USAXS results from ceramic coatings to display its capability of resolving anisotropic scattering patterns (Ilavsky *et al.*, 2002). In thermally sprayed (TS) or electron-beam (EB) physical

vapor-deposited (PVD) yttria-stabilized zirconia (YSZ) coatings (8% mass Y_2O_3 in ZrO_2), the void microstructures control their properties and performance. Some of the interlamellar and intralamellar cracks and intercolumnar voids are anisotropic and exhibit a large size range. The fragile nature of these coatings makes electron microscopy measurements difficult. The microstructure of EB-PVD coatings is particularly complex. However, by using two-dimensional collimated USAXS, we have studied successfully and quantified the microstructures responsible for the anisotropic scattering of EB-PVD coatings (Kulkarni *et al.*, 2006; Renteria *et al.*, 2007). Here we present in Fig. 6 anisotropic data taken at $q = 2.6 \times 10^{-4}, 1.0 \times 10^{-3}$ and 9.0×10^{-3} Å^{-1}. The scattering from large voids is strong in the direction parallel to the substrate, and the scattering from the small voids shows a more complex orientation distribution. The large features within the microstructures are intercolumnar pores, which are preferentially perpendicular to this surface, whereas the small features are intracolumnar growth-related voids, which are very difficult, if not impossible, to characterize by other methods. Their orientation is, as our results indicate for this sample, tilted towards the substrate surface.

The polar plots also show predicted anisotropies at each q. These are derived from a model multi-component void microstructure, for which the microstructural parameters (void size, shape, volume fraction and anisotropy distributions) have been obtained by simultaneously fitting multiple two-dimensional collimated USAXS data sets [$I(q)$ *versus* q] measured both in different azimuthal directions of **q** (*i.e.* different α) and for different orthogonal orientations of the sample within the X-ray beam. As far as we are aware, this degree of multi-component, anisotropic, quantitative, microstructural information, extending over the length scale from ~10 nm to more than 1 µm, is not obtainable by any other means.

7.4. Selected-area USAXS

Fig. 7 shows an example of selected-area USAXS. The sample system is a solid-oxide fuel cell (SOFC). Its SEM (scanning electron microscopy) image is shown in the inset. The lanthanum strontium manganite (LSM) cathode and the Ni/YSZ cermet anode are separated by a thin, dense YSZ electrolyte layer. Both the top layer (cathode) and the bottom layer (anode) are porous. However, the detailed void morphologies are different and may change during service life, affecting the SOFC electrochemical and mechanical properties, and hence performance. After surveying the sample into position using the USAXS instrument's X-ray camera, sample positions could be set up for selected-area two-dimensional collimated USAXS scans, shown by the circled positions in the fuel cell. Using the maximum entropy method (Potton *et al.*, 1988) and allowing for the different scattering contrasts in the cathode and anode, we obtained the void size distributions at each of the three sample positions. The three positions have different levels of porosity and some difference in pore size distribution. While Fig. 7 is purely illustrative, selected-area

USAXS measurements can be made using much smaller beam sizes (down to a few micrometres) that allow microstructure gradients to be interrogated. Such studies are made possible by the instrument's precision control of the sample stage (10 nm) and the detector stage (2.5 µm) motions, and the ability to interchange the USAXS photodiode and X-ray imaging camera without disturbing the instrument geometry.

7.5. Anomalous USAXS

Fig. 8 shows an example of anomalous USAXS from silicon nitride. Silicon nitride is a ceramic material consisting of Si_3N_4 matrix grains and crystalline additive secondary phases. Characterization of the microstructure is complicated by the
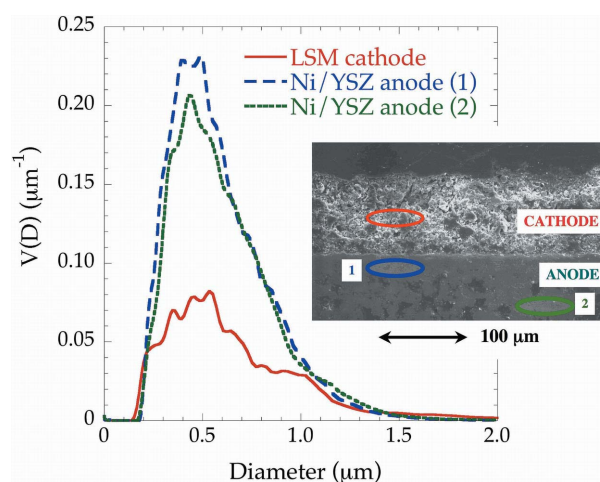

Figure 7
An example of selected-area USAXS results for volume distribution of voids. The inset shows a SEM image near an interface within a solid-oxide fuel cell. The circled regions in the micrograph indicate the scattering volumes for which the pore size distribution curves were derived.
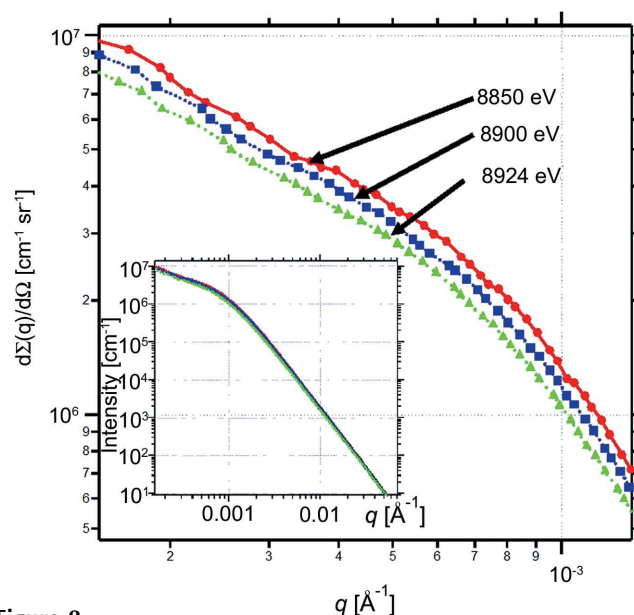

Figure 8
An example of anomalous USAXS scattering data from silicon nitride containing a $Yb_2Si_2O_7$ secondary phase at −0.094, −0.044 and −0.020 keV from the Yb L_{III} absorption edge (8.944 keV).

fact that the scattering contrasts and the sizes of secondary phases and voids can be very similar. The main secondary phase in commercial grade SN88 is $Yb_2Si_2O_7$. We performed anomalous USAXS measurements at 8.850, 8.900 and 8.924 keV near the Yb L_{III} absorption edge (8.944 keV), as shown in Fig. 8. The data show strong scattering over the range $0.0002 < q < 0.05$ Å^{-1}. The transition between Guinier and Porod scattering in the vicinity of $q \simeq 0.001$ Å^{-1} was visible, thanks to the low-q capability of the USAXS instrument. At $q < 0.005$ Å^{-1}, the variation of measured intensity with energy is consistent with the variation of scattering contrast with energy for $Yb_2Si_2O_7$, while for $q > 0.01$ Å^{-1}, the variation with energy is less distinct. From measurements on samples of SN88 with varying amounts of applied creep strain, and using our A-USAXS data analysis method (Jemian et al., 1991), we determined that the population distribution of creep porosity was similar in size (100–600 nm) to that of the secondary phase, while the volume fraction of the creep porosity was a linear function of the applied creep strain. For samples of commercial silicon nitride SN281, where Yb is replaced by Lu, the volume fraction of the creep porosity determined from A-USAXS measurements was remarkably close to zero (Lofaj et al., 2001).

7.6. One-dimensional collimated USAXS of particles with great size asymmetry

Nanoparticle colloidal haloing is a new stabilization mechanism for colloidal dispersions. The solution mixture contains negligibly charged micrometre-sized colloidal particles and highly charged nanoparticles. The nanoparticles stabilize the binary solution by forming a 'halo' layer around the microspheres. Because of the large size and charge asymmetry of the particles in solution, the structure of the halo has remained a mystery. The distribution of zirconia nanoparticles near the surface of silica microspheres was studied using one-dimensional collimated USAXS (Zhang, Long, Jemian et al., 2008). The slit-smeared USAXS profiles of

silica microspheres, zirconia nanoparticles and the mixtures are shown in Fig. 9. Our analysis shows that the nanoparticles self-organize into a halo (or shell) that resides at a separation distance of ~2 nm from the microsphere surface, which is very close to the value of the Debye screening length. It was also found that the nanoparticle concentration within this shell is significantly enriched relative to its bulk value in solution, yet the lateral separation distance between nanoparticles within each halo greatly exceeds their characteristic size. This research was able to resolve quantitatively the distribution of nanoparticles in the halo by making use of the very wide q range of the APS USAXS.

7.7. USAXS imaging of low-contrast, distributed nanoscale structures

An example of USAXS imaging is given in Fig. 10, which shows a USAXS image ($q = 0.0005$ Å^{-1}) of a three-dimensional conductive network of self-assembled carbon black nanowires embedded in poly(methyl methacrylate) (PMMA) (Levine et al., 2007). Stereo images show that these wires assemble on the triple junctions of PMMA Voronoi cells that form during elevated-temperature compression of the starting PMMA and carbon black powders. One-dimensional collimated USAXS scans from the same sample determined that the mean wire diameter is 31 nm. Although the spatial resolution of these images is only about 2 µm, the nanowires show up clearly since they are distributed over much larger distances.

8. Conclusion

The versatile ultra-small-angle X-ray scattering (USAXS) instrument at the Advanced Photon Source (APS) at Argonne National Laboratory is a fundamental characterization facility
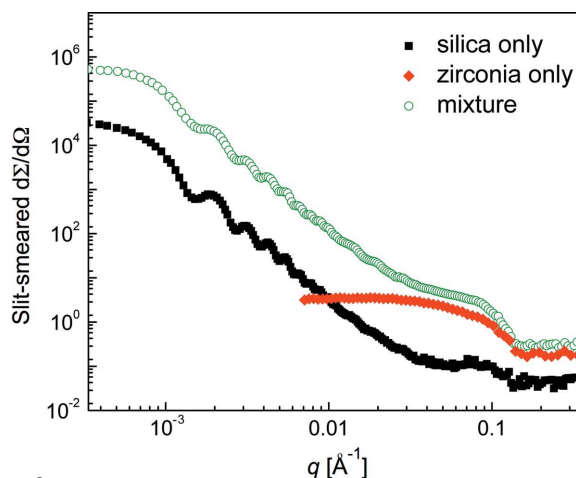
Figure 9
Measured slit-smeared USAXS profiles of silica microspheres, zirconia nanoparticles and the colloidal mixture including nanoparticle stabilization.
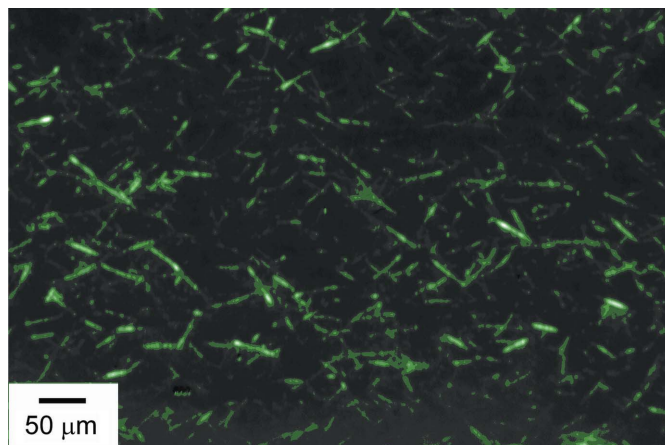
Figure 10
A USAXS image acquired from a composite sample of interconnected linear arrangements of nanoscale carbon black (CB) particles (1% mass fraction) that decorate triple junctions within press-sintered amorphous poly(methyl methacrylate). The bright linear features are the self-assembled CB nanowires. *In situ* USAXS and USAXS imaging revealed that the conducting wires have lengths ranging from 10 to 100 µm and sample-averaged diameters down to 24 nm (Levine et al., 2007).

that is optimized for the high brilliance and low emittance of an APS undulator source. Its angular and energy resolutions of 10^{-4}, its accurate and repeatable X-ray energy tunability over its operational energy range from 8 to 18 keV, and its excellent signal-to-noise ratio support a wide range of problems, from addressing the fundamental scientific issues in soft matter to characterization of shocked and explosive materials. It makes use of primary calibration of X-ray scattering cross sections, a scattering vector range from 0.0001 to 1 Å^{-1}, and stability and reliability over extended running periods. With one-dimensional collimated (slit-smeared) USAXS, two-dimensional collimated USAXS and USAXS imaging, it can be optimally configured for either isotropic or anisotropic scattering. The associated data reduction and data analysis package brings online, real-time data analysis to the user, as well as more sophisticated support for detailed analyses. USAXS delivers a statistical view of the scattering microstructures, and the USAXS imaging makes possible the complementary analysis of individual structures and inhomogeneous microstructures.

References

Agamalian, M., Christen, D. K., Drews, A. R., Glinka, C. J., Matsuoka, H. & Wignall, G. D. (1998). *J. Appl. Cryst.* **31**, 235–240.

Aizawa, K. & Arai, M. (2006). *Phys. B Condens. Matter*, **385–386**, 1114–1117.

Aizawa, K. & Tomimitsu, H. (1995). *Phys. B*, **213**, 884–886.

Allen, A. J., Hackley, V. A., Jemian, P. R., Ilavsky, J., Raitano, J. M. & Chan, S.-W. (2008). *J. Appl. Cryst.* **41**, 918–929.

Allen, A. J., Jemian, P. R., Black, D. R., Burdette, H. E., Spal, R. D., Krueger, S. & Long, G. G. (1994). *Nucl. Instrum. Methods Phys. Res. Sect. A*, **347**, 487–490.

Barker, J. G., Glinka, C. J., Moyer, J. J., Kim, M. H., Drews, A. R. & Agamalian, M. (2005). *J. Appl. Cryst.* **38**, 1004–1011.

Beaucage, G. (1995). *J. Appl. Cryst.* **28**, 717–728.

Bonse, U. & Hart, M. (1965). *Appl. Phys. Lett.* **7**, 238–240.

Bonse, U. & Hart, M. (1966). *Z. Phys.* **189**, 151–162.

Borbely, S., Heiderich, M., Schwahn, D. & Seidl, E. (2000). *Phys. B*, **276**, 138–139.

Carpenter, J. M., Agamalian, M., Littrell, K. C., Thiyagarajan, P. & Rehm, Ch. (2003). *J. Appl. Cryst.* **36**, 763–768.

Cerbino, R., Peverini, L., Potenza, M. A. C., Robert, A., Bosecke, P. & Giglio, M. (2008). *Nat. Phys.* **4**, 238–243.

Chu, B., Li, Y. & Gao, T. (1992). *Rev. Sci. Instrum.* **63**, 4128–4133.

Chu, B., Yeh, F., Li, Y., Harney, P. J., Rousseau, J., Darovsky, A. & Siddons, D. P. (1994). *Rev. Sci. Instrum.* **65**, 3233–3237.

Cotton, J. P. (1991). Editor. *Initial Data Treatment: Neutron, X-ray and Light Scattering*. Amsterdam: North Holland.

Dalesio, L. R., Kraimer, M. R. & Kozubal, A. J. (1993). EPICS Architecture, http://www.aps.anl.gov/epics/docs/general.php.

Debye, P. & Bueche, A. M. (1949). *J. Appl. Phys.* **20**, 518–525.

Hainbuchner, M., Villa, M., Kroupa, G., Bruckner, G., Baron, M., Amenitsch, H., Seidl, E. & Rauch, H. (2000). *J. Appl. Cryst.* **33**, 851–854.

Ilavsky, J., Allen, A. J., Long, G. G. & Jemian, P. R. (2002). *Rev. Sci. Instrum.* **73**, 1660–1662.

Ilavsky, J. & Jemian, P. R. (2009). *J. Appl. Cryst.* **42**, 347–353.

Ilavsky, J., Jemian, P. R., Allen, A. J. & Long, G. G. (2003). *AIP Conference Proceedings Volume 705: Synchrotron Radiation Instrumentation, Eighth International Conference on Synchrotron Radiation Instrumentation*, pp. 510–513. Melville: American Institute of Physics.

Jemian, P. R. (1990). PhD thesis, Northwestern University, IL, USA.

Jemian, P. R. & Long, G. G. (1990). *J. Appl. Cryst.* **23**, 430–432.

Jemian, P. R., Weertman, J. R., Long, G. G. & Spal, R. D. (1991). *Acta Metall. Mater.* **39**, 2477–2487.

Kammler, H. K., Beaucage, G., Mueller, R. & Pratsinis, S. E. (2004). *Langmuir*, **20**, 1915–1921.

Krosigk, G. V., Cunis, S., Gehrke, R. & Kranold, R. (2001). *Nucl. Instrum. Methods Phys. Res. Sect. A*, **467**, 1088–1091.

Kulkarni, A., Goland, A., Herman, H., Allen, A. J., Dobbins, T., DeCarlo, F., Ilavsky, J., Long, G. G., Fang, S. & Lawton, P. (2006). *Nucl. Instrum. Methods Phys. Res. Sect. A*, **426**, 43–52.

Lai, B., Khounsary, A., Savoy, R., Moog, L. & Gluskin, E. (1993). *Undulator A Characteristics and Specifications*. Advanced Photon Source, Argonne National Laboratory, IL, USA.

Lake, J. A. (1967). *Acta Cryst.* **23**, 191–194.

Levine, L. E. & Long, G. G. (2004). *J. Appl. Cryst.* **37**, 757–765.

Levine, L. E., Long, G. G., Ilavsky, J., Gerhardt, R. A., Ou, R. & Parker, C. A. (2007). *Appl. Phys. Lett.* **90**, 014101.

Lofaj, F., Wiederhorn, S. M., Long, G. G. & Jemian, P. R. (2001). *Ceram. Eng. Sci. Proc.* **22**, 167–174.

Long, G. G., Jemian, P. R., Weertman, J. R., Black, D. R., Burdette, H. E. & Spal, R. (1991). *J. Appl. Cryst.* **24**, 30–37.

Long, G. G. & Levine, L. E. (2005). *Acta Cryst.* A**61**, 557–567.

Long, G. G., Levine, L. E. & Fields, R. J. (2001). *Mater. Sci. Eng. A Struct. Mater.* **309**, 28–31.

Narayanan, T., Diat, O. & Bosecke, P. (2001). *Nucl. Instrum. Methods Phys. Res. Sect. A*, **467**, 1005–1009.

Parratt, L. G. (1954). *Phys. Rev.* **95**, 359–369.

Potton, J. A., Daniell, G. J. & Rainford, B. D. (1988). *J. Appl. Cryst.* **21**, 663–668.

Renteria, A. F., Saruhan, B., Ilavsky, J. & Allen, A. J. (2007). *Surf. Coat. Technol.* **201**, 4781–4788.

Rieker, T. P. & Hubbard, P. F. (1998). *Rev. Sci. Instrum.* **69**, 3504–3509.

Schaefer, D. W., Brown, J. M., Anderson, D. P., Zhao, J., Chokalingam, K., Tomlin, D. & Ilavsky, J. (2003). *J. Appl. Cryst.* **36**, 553–557.

Schelten, J. & Schmatz, W. (1980). *J. Appl. Cryst.* **13**, 385–390.

Schwahn, D. & Koo, M. H. (1986). *Studies of Heterogeneities of Micrometer-Range with Double Crystal Diffractometer, Atomic Transport and Defects in Metals by Neutron Scattering*, edited by W. P. C. Janot, D. Richter & T. Springer, pp. 83–88. Berlin: Springer-Verlag.

Schwahn, D., Miksovsky, A., Rauch, H., Seidl, E. & Zugarek, G. (1985). *Nucl. Instrum. Methods Phys. Res. Sect. A*, **239**, 229–234.

Shinohara, Y., Kishimoto, H., Inoue, K., Suzuki, Y., Takeuchi, A., Uesugi, K., Yagi, N., Muraoka, K., Mizoguchi, T. & Amemiya, Y. (2007). *J. Appl. Cryst.* **40**, s397–s401.

Shu, D., Toellner, T. S. & Alp, E. E. (2001). *Nucl. Instrum. Methods Phys. Res. Sect. A*, **467–468**, 771–774.

Smolsky, I. L., Liu, P., Niebuhr, M., Ito, K., Weiss, T. M. & Tsuruta, H. (2007). *J. Appl. Cryst.* **40**, s453–s458.

Swislow, G. (2009). *Spec.* Certified Scientific Software, Cambridge, Massachusetts, USA, http://www.certif.com/spec.html.

Sztucki, M., Gorini, J., Vassalli, J.-P., Goirand, L., van Vaerenbergh, P. & Narayanan, T. (2008). *J. Synchrotron Rad.* **15**, 341–349.

Zhang, F., Long, G. G., Jemian, P. R., Ilavsky, J., Milam, V. T. & Lewis, J. A. (2008). *Langmuir*, **24**, 6504–6508.

Zhang, F., Long, G. G., Levine, L. E., Ilavsky, J. & Jemian, P. R. (2008). *J. Appl. Cryst.* **41**, 416–427.